# Unveiling and controlling the electronic structure of oxidized semiconductor surfaces: Crystalline oxidized InSb(100)(1 × 2)-O

J. J. K. Lång,[1] M. P. J. Punkkinen,[1] M. Tuominen,[1] H.-P. Hedman,[2] M. Vähä-Heikkilä,[2] V. Polojärvi,[3] J. Salmi,[3] V.-M. Korpijärvi,[3] K. Schulte,[4] M. Kuzmin,[1,5] R. Punkkinen,[2] P. Laukkanen,[1,*] M. Guina,[3] and K. Kokko[1]

[1]*Department of Physics and Astronomy, University of Turku, FI-20014 Turku, Finland*

[2]*Department of Information Technology, University of Turku, FI-20014 Turku, Finland*

[3]*Optoelectronics Research Centre, Tampere University of Technology, FI-33101 Tampere, Finland*

[4]*MAX-lab, Lund University, SE-221 00 Lund, Sweden*

[5]*Ioffe Physical-Technical Institute of the Russian Academy of Sciences, St. Petersburg 194021, Russian Federation*

(Received 15 October 2013; revised manuscript received 7 July 2014; published 29 July 2014)

The exothermic nature of oxidation causes nearly all semiconductor applications in various fields like electronics, medicine, photonics, and sensor technology to acquire an oxidized semiconductor surface part during the application manufacturing. The significance of understanding and controlling the atomic scale properties of oxidized semiconductor surfaces is expected to increase even further with the development of nanoscale semiconductor crystals. The nature of oxidized semiconductor layers is, however, hard to predict and characterize as they are usually buried and amorphous. To shed light on these issues, we pursue a different approach based on oxidized III-V semiconductor layers that are crystalline. We present a comprehensive characterization of oxidized crystalline InSb(100)(1 × 2)-O layers by *ab initio* calculations, photoelectron spectroscopy, scanning tunneling microscopy, and spectroscopy, and demonstrate the electronic band structures of different oxidized phases of the semiconductor, which elucidate the previous contradictory semiconductor-oxidation effects. At 0.5 monolayer (ML) oxidation, oxygen atoms tend to occupy subsurface Sb sites, leading to metallic states in the semiconductor band gap, which arise from top dimers. When the oxidation is increased to the 1.0–2.0 ML concentration, oxygen occupies also interstitial sites, and the insulating band structure without gap states is stabilized with unusual occupied In dangling bonds. In contrast, the 2.5–3.0 ML oxide phases undergo significant changes toward a less ordered structure. The findings suggest a methodology for manipulating the electronic structure of oxidized semiconductor layers.

DOI: 10.1103/PhysRevB.90.045312 PACS number(s): 73.20.At, 73.20.Hb, 81.65.Mq

## I. INTRODUCTION

Atomically well-defined surfaces of crystals often undergo significant spontaneous structural transformations, relaxation, and/or reconstruction in clean ultrahigh vacuum (UHV) conditions. The driving forces behind these processes and the structural building blocks of the reconstructed and relaxed surfaces are well understood for many materials [1]. When the crystals are exposed to an oxygen-containing environment, oxidized surface layers readily form on most metal and semiconductor materials (e.g., Ge, Si, compounds of III-V and II-VI). The physical properties (e.g., electronic structures) of the resulting surface-oxide phases are of great fundamental interest and play a significant role in applications in many fields like catalysis [2–5], electronics [6,7], material protection [8,9], medicine [10,11], and photonics [12,13]. Furthermore, the strive toward decreasing material dimensions in technology leads simultaneously to increasing significance of the properties of oxidized surface parts at the atomic scale because the surfaces form such a crucial part of the nanoscale materials. However, the properties of the oxidized surfaces are, in general, less understood than those of clean crystals because the oxidized phases are typically amorphous, making atomic-scale studies challenging.

The discovered crystalline phases of surface oxides for some metals have indeed been helpful for understanding phenomena of oxidized metal surfaces [2–5,8,9]. In contrast, the lack of crystalline phases has hindered the understanding of oxidized semiconductor surfaces which further affect the functionality of semiconductor-based devices of electronics, photonics, and sensor technology, for instance [2,6,7,11–22]. Even, the composition and electronic structure of the revolutionary oxidized silicon surfaces, i.e., $SiO_x/Si$, are still under discussion because of the amorphous structure of $SiO_x$.

Thus, the recently found crystalline oxidized surfaces of III-V compound semiconductors (e.g., GaAs, InAs, InSb) provide an alternative well-defined platform, a model system for the studies [23]. The first atomic models have been suggested for crystalline oxide phases of InAs [23]. However, no electronic band structure has been so far reported for these oxidized materials. The understanding of the electronic structures is in turn important to understand many phenomena such as adsorption, transport, and recombination of electrons as well as photon emission. On the other hand, the electronic structures of the oxidized III-V semiconductors in particular have become more and more important because, after decades of intense research and development (e.g., Refs. [6,7,24–32]), the III-V channel metal-oxide-semiconductor field-effect transistors (MOSFET) are now on the roadmap of microelectronics manufacturers. Concerning the realization of this potential technology, one remaining problem is still the gate oxide/III-V interface of the carrier channel. The III-V surfaces become easily oxidized, as

*pekka.laukkanen@utu.fi

 ©2014 American Physical Society

mentioned above, due to the energetically favored oxidation and the practical difficulty to avoid the contact of III-V surfaces with oxygen during manufacturing the oxide/semiconductor junction for applications. The III-V oxidation is commonly considered to result in a poor quality interface layer with a high density of defect states around the III-V band gap, which leads to a reduced electric current and a nonradiative recombination, for example. In the first approximation, the phenomenon can be summarized as follows: (i) oxidation causes a structural disorder leading to the formation of point defects and deviation in bonding, and (ii) oxygen incorporation into a semiconductor causes a modified electronic structure and produces an oxide phase with unwanted electronic states tailing across the band gap. Indeed, much work has been done to understand and control/reduce these harmful oxidation-induced effects. The control techniques include the sulfur passivation of III-V surfaces, depositing silicon interface layer, growth of epitaxial oxides, and removal of surface oxides via the self-cleaning effect in atomic layer deposition (ALD) of oxides [7,25,30,33–35]. Furthermore, harmful electron states have been linked, amongst others, to group-V dimers (pairs); group-V and group-III dangling bonds (missing bonds); and III-$O_x$ or V-$O_x$ phases [7,27,29–31]. Meanwhile, certain forms of semiconductor oxides (e.g., $Ga_2O$ and $InAsO_x$) have been observed to be nonharmful or even to improve the electrical properties of the oxide/semiconductor interfaces [27,28]. The beneficial crystalline $InAsO_x$ surface oxide of InAs(100) was obtained by a surprising method, namely by oxidizing InAs(100) in nearly atmospheric pressure prior to an oxide film growth [28], in contrary to the common target to minimize the III-V surface oxidation. This result appears to be consistent with an almost simultaneous finding of the formation of the crystalline oxidized III-V surface layers via proper oxidation in UHV-based environment [23]. These results thus suggest that, after all, proper oxidation conditions of III-V surfaces can work like the miraculous Si oxidation. Such a preoxidation approach is clearly supported by the recent findings of Wang *et al.* [32] for $HfO_2$/InAs: engineering one of the crystalline oxidized III-V structures, namely InAs(100)(3 × 1)-O on the InAs(100) before the $HfO_2$ deposition improves the interface significantly.

To shed light on the oxidation-induced changes in the electronic band structures of semiconductors, we have utilized the oxidized crystalline III-V surfaces [23]. We exploit complementary measurements alongside *ab initio* calculations to determine first the atomic structures for the oxidized and (1 × 2)-reconstructed InSb(100) surfaces, enabling a detailed analysis of the electronic band structures. This InSb(100)(1 × 2)-O surface was chosen as a starting point for the detailed analysis because it has a small unit cell that allows complex calculations with a large parameter space within reasonable

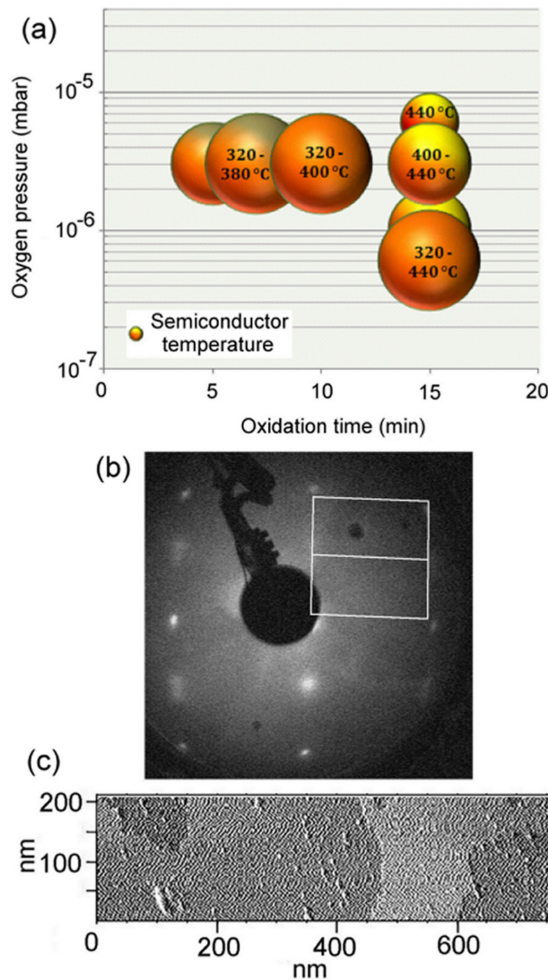


FIG. 1. (Color online) (a) Spheres mark the oxidation conditions found for InSb(100)(1 × 2)-O. (b) LEED pattern from InSb(100)(1 × 2)-O: white square marks the lattice of the (1 × 1) bulk plane, and white rectangle is the lattice of surface superstructure. (c) Large-scale empty-state STM image from InSb(100)(1 × 2)-O taken with 1.67 V and 0.05 nA.

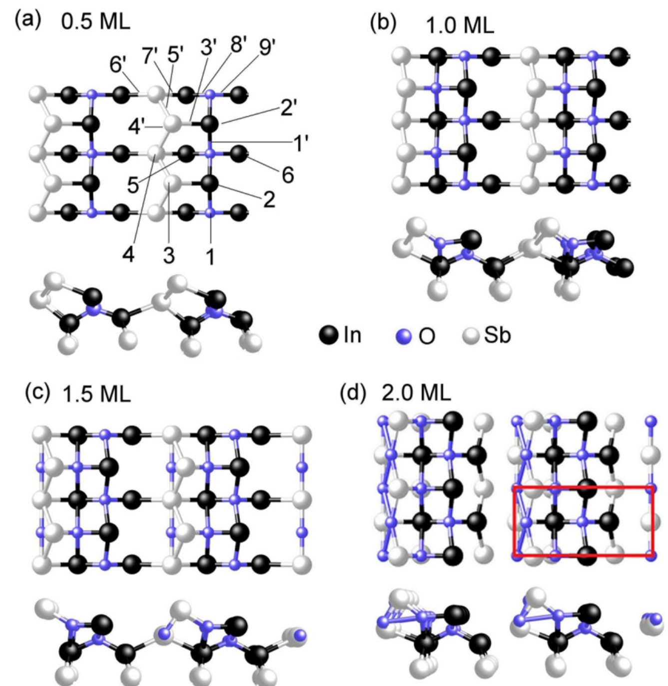


FIG. 2. (Color online) (a) Stable (1 × 2) model with 0.5 ML of oxygen. The oxygen sites are numbered. (b)–(d) Stable 1.0, 1.5, and 2.0 ML atomic models, respectively.

time. The presented results demonstrate unexpected oxidation-induced changes in the electronic structures of the oxidized semiconductors, which elucidate origins of the previously observed harmful and nonharmful effects of the semiconductor oxidation.

## II. METHODS

Surface-science experiments were performed in two separate UHV systems. High-resolution synchrotron-radiation x-ray photoelectron spectroscopy (SR-XPS) was done at the MAX-lab (Sweden) on beamline I311. Scanning tunneling microscopy and spectroscopy (STM/STS) were performed with Omicron equipment. Both systems were equipped with a low-energy electron diffraction (LEED) unit. $N$-type InSb(100) substrate pieces were cleaned by Ar sputtering which produced the well-defined InSb(100)$c(8 \times 2)$ starting surface after the postheating around 450 °C. Several cycles, typically five cycles of the sputtering and postheating, were employed to obtain a sharp $c(8 \times 2)$ LEED. The Ar pressure was $5-10 \times 10^{-7}$ mbar during sputtering with 1 kV and 10 mA. The pristine InSb(100)$c(8 \times 2)$ surface was oxidized by introducing the $O_2$ gas into a vacuum chamber via a leak valve (the substrate faced the leak valve).

For a capacitor test, $SiO_2$ cap layers (∼3 nm) were deposited on preoxidized and clean InSb surfaces *in situ* in the same UHV system, and subsequently, $Al_2O_3$ films (15 nm) were *ex situ* deposited with a separate ALD system. The 50-nm-thick Ni gate-metal contacts (250 $\mu$m diameter) were evaporated through shadow mask, and the back contact was Ni/Au/Ge/Au. Capacitors were postheated at 300 °C in nitrogen flow for 15 min. Capacitance-voltage (CV) measurements were carried out by using a LCR precision meter (HP4284A) at room temperature.

Theoretical calculations were performed using *ab initio* density functional total energy method within the local density approximation (LDA). The approach is based on a plane wave basis set and projector-augmented wave method (Vienna *Ab initio* Simulation Package, VASP). The oxidized InSb(100) surfaces were modeled by using $(1 \times 2)$ and $(4 \times 2)$ pseudohydrogenated supercells of 17 atomic layers, separated by a vacuum of 18 Å wide. Two bottom layers were fixed while other atoms including pseudohydrogens were relaxed until the remaining forces were less than 20 meV/Å. The k-point sampling was performed by the Monkhorst-Pack scheme with the origin shifted to the $\Gamma$ point. $2 \times 4 \times 1$ and $6 \times 3 \times 1$ k-point grids were used for the $(4 \times 2)$ and $(1 \times 2)$ slabs, respectively. The plane wave cutoff energy was 400 eV. Theoretical lattice constant of 6.47 Å was used for InSb. Surface energies were evaluated as a function of O and In chemical potentials. Simulated annealing calculations were employed for the structure optimization by annealing the four top-most atomic layers (the position of the other layers were kept fixed) from 300 to 1000 K within 3 ps and subsequently keeping the temperature at 1000 K for another 3 ps. Finally, the temperature was cooled from 1000 to 300 K within 3 ps, and the found structures were then relaxed by traditional density functional theory (DFT) calculations. To contemplate the oxidation-induced bands relative to the bulk band structure, Heyd-Scuseria-Ernzerhof (HSE)06 hybrid exchange-correlation functionals were used for accurate band structure calculations where 59-Å-thick slabs with $(1 \times 2)$ symmetry and 33 Å of vacuum were used. For these calculations, we used a 0.25 fraction of $\alpha$ of the Hartree-Fock exchange and 21 k-points along the high symmetry directions of the surface Brillouin zone.

## III. RESULTS AND DISCUSSION

Figure 1 summarizes the oxidation conditions that provided a $(1 \times 2)$ LEED pattern. Figure 1 also exemplifies a typical large-scale STM image for a well-ordered InSb(100)$(1 \times 2)$-O

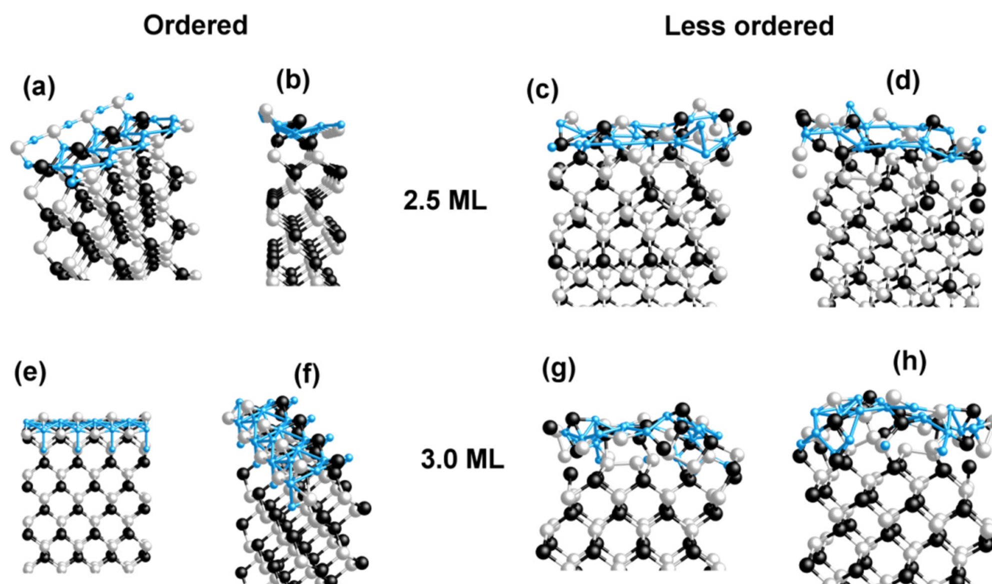


FIG. 3. (Color online) Two different views (a) and (b) for the ordered and (c) and (d) for less ordered models of the InSb(100)$(1 \times 2)$-O surface with 2.5 ML of oxygen. Two different views (e) and (f) for the ordered and (g) and (h) less ordered models of the InSb(100)$(1 \times 2)$-O surface with 3.0 ML of oxygen.

surface, which reveals a smooth two-dimensional island-step structure, consistent with the presence of a long-range ordered surface structure observed by LEED.

To explain the apparent stability of a crystalline InSb(100)(1 × 2)-O surface layer, we turn to calculations exploring energetically favorable structures (Fig. 2) with a 0.5 to 2 ratio of O:InSb in the surface. The overall composition of the (1 × 2) cells in this range is $In_3Sb_2O_x$, where $x = 1, 2, 3$, or 4 for the 0.5, 1.0, 1.5, and 2.0 O:InSb ratios or monolayers (ML), respectively. At the 0.5 ML oxidation, the energy is minimized when oxygen replaces subsurface Sb sites [labeled 1 in Fig. 2(a)], and the surface dimer composition is In-Sb. This oxygen site is substantially more stable, 0.18 eV/(1 × 1) than any other site including interstitials at 0.5 ML. As expected, the energy is further decreased when the oxidation proceeds to 1.0 ML and above it. At the 1.0 ML oxidation [Fig. 2(b)], oxygen also occupies the interstitial site 3′. The occupancy of interstitial sites is plausible because of a small atomic size of oxygen with respect to the InSb lattice parameters. This finding also agrees with the previous results for the GaAs oxidation [31]. The characteristic of the 1.0 ML model is that the interstitial oxygen protrudes downwards making bonds with third-layer In atoms. Figures 2(c) and 2(d) show the energetically favored models at the 1.5 and 2.0 ML oxidations, respectively. The latter (1 × 2) cell includes locally InO, $InO_3$, $SbO_2$, and $SbO_3$ type bondings [Fig. 2(d)]. The simulated annealing up to 1000 K did not significantly change the atomic structures at 0.5–2.0 ML, indicating that the presented models are indeed low energy structures. In contrast, ordered models with the 2.5 ML and higher oxidations are metastable and undergo significant structural changes toward a less ordered structure due to the annealing. Figure 3 exemplifies these annealing-induced structural changes for the 2.5 and 3.0 ML oxide phases. For example, at the 2.5 ML concentration, the disordered model is 0.57 eV/(1 × 1) lower in energy compared with the corresponding ordered model.

Figure 4 shows zoomed STM images measured from the InSb(100)(1 × 2)-O surface and the simulated STM images based on the ordered models with 0.5–2.0 ML of oxygen. The surface is characterized by rows along the [0-11] crystal direction with 0.9 nm separation, consistent with the distance of two times the InSb lattice constant. In general, the simulated images agree reasonably with the measured images, but more detailed, low-temperature STM measurements are needed to

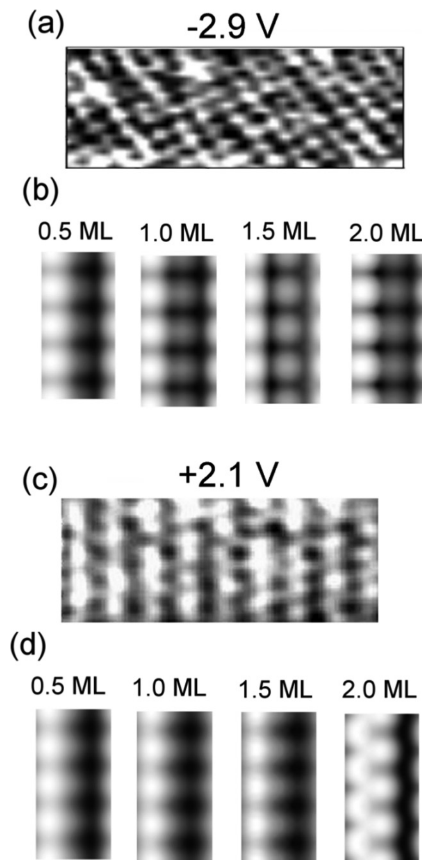


FIG. 4. (a) Filled-state zoomed STM image measured from InSb(100)(1 × 2)-O; the tunneling current is 0.1 nA and the voltage is −2.9 V. (b) Simulated filled-state (−2.9 V) STM images for the energetically favored models with different oxygen concentrations. (c) Empty-state zoomed STM image measured from InSb(100)(1 × 2)-O; the tunneling current is 0.05 nA and the voltage is +2.1 V. (d) Simulated empty-state (+2.1 V) STM images for the energetically favored models with different oxygen concentrations.

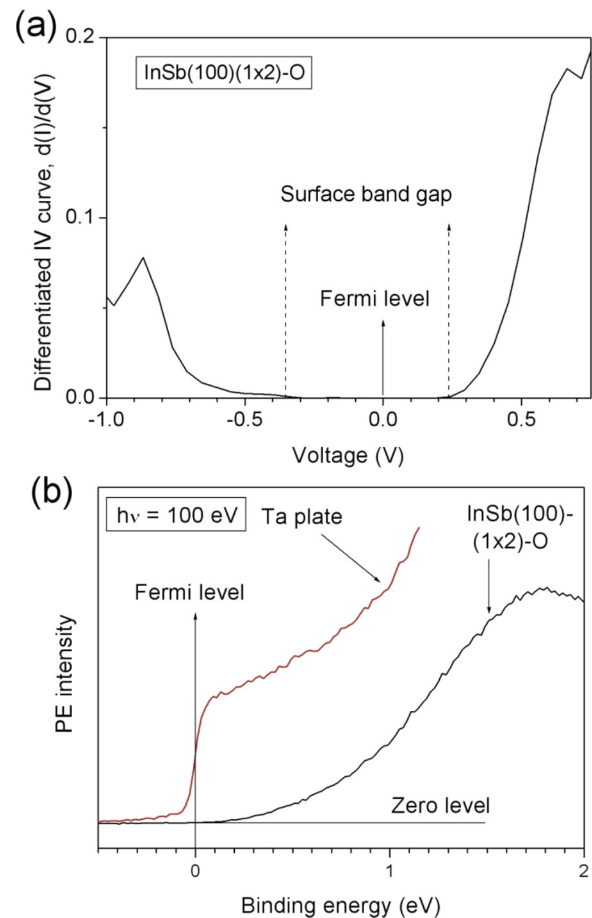


FIG. 5. (Color online) (a) Differentiated STS curve of InSb(100)(1 × 2)-O. (b) Valence-band photoemission from InSb(100)(1 × 2)-O alongside the Fermi edge measured on a Ta plate in electrical contact with the InSb.

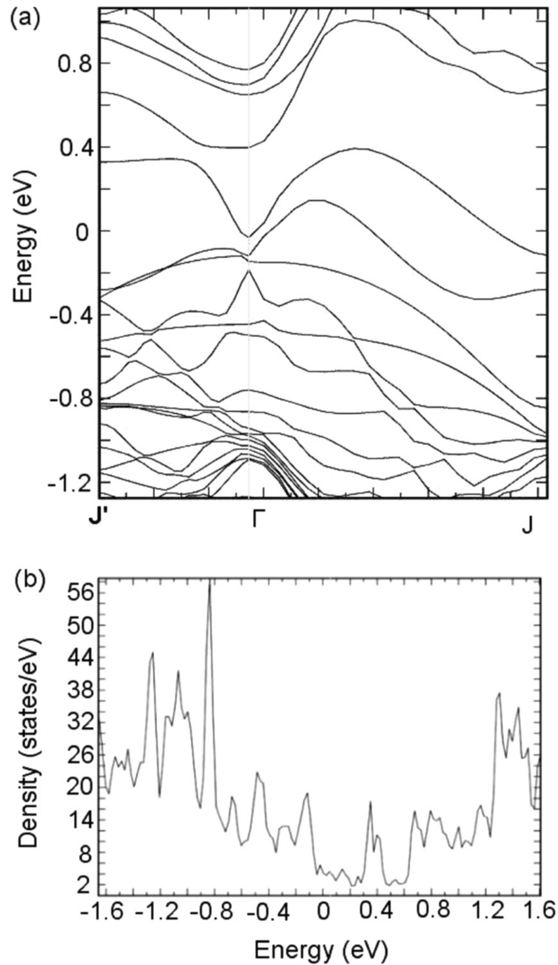


FIG. 6. (a) The calculated band structure of InSb(100)(1 × 2)-O at 0.5 ML of oxygen. (b) The corresponding density of states spectrum.

distinguish the most likely model on the basis of STM images. It is surprising how similar STM images these different models provide (expect for the empty-state one of the 2.0 ML model).

A well-ordered InSb(100)(1 × 2)-O surface is semiconducting, as can be concluded from the STS curve in Fig. 5(a) and from photoemission measurements in Fig. 5(b), because there is no intensity (i.e., density of states) at the Fermi level. The STS spectrum in Fig. 5(a) shows that the surface energy gap of InSb(100)(1 × 2)-O is about 0.6 eV. However, the calculations reveal that the structures at 0.5 ML oxidation, including that in Fig. 2(a), are metallic (i.e., bands or intensity at the Fermi level) as presented in Fig. 6. The dimer sites In-2 and Sb-3 supply the main contribution to these metallic states. Indeed, the semiconductor oxidation has been commonly considered to cause harmful gap states.

Therefore, it is remarkable that the surface reverts to semiconducting with a clear band gap when InSb is further oxidized to 1.0–2.0 ML, as shown in Fig. 7, consistent with our measurements. Figure 7(a) shows a band along the $J$-Γ direction associated with the topmost Sb with its corresponding weight illustrated by blue squares. Even the second layer Sb atoms (site 4) contribute a nonnegligible weight to the band. This kind of group-V antibonding band seems to be a plausible candidate for harmful gap states. However, employment of the LDA functional is known to underestimate the gaps. Although the slab calculations open the gap, the exact position of the Sb-related band relative to the bulk gap remains speculative. Therefore, we also studied the oxidized InSb with hybrid exchange-correlation functionals. As presented in Fig. 7(b), these calculations show a band gap of 0.26 eV, close to the known InSb gap. The Sb-related band [green symbols in Fig. 7(b)] now locates 0.45 eV above the conduction band minimum. For the InSb(100)(1 × 2)-O surface oxidized to 2.0 ML, this band disappears or moves upward as it is not found in the calculated energy window [Fig. 7(c)].

A powerful tool to examine bonds and their characteristics in molecules and solids is the electron localization function (ELF). It gives information about the spatial localization of electron pairs in an atomic system and is described by the pair probability of finding an electron in the vicinity of a reference electron with the same spin. We utilized ELF to study the bond characteristic of the InSb(100)(1 × 2)-O models. Figure 8(a) shows a two-dimensional ELF plot along the plane spanned

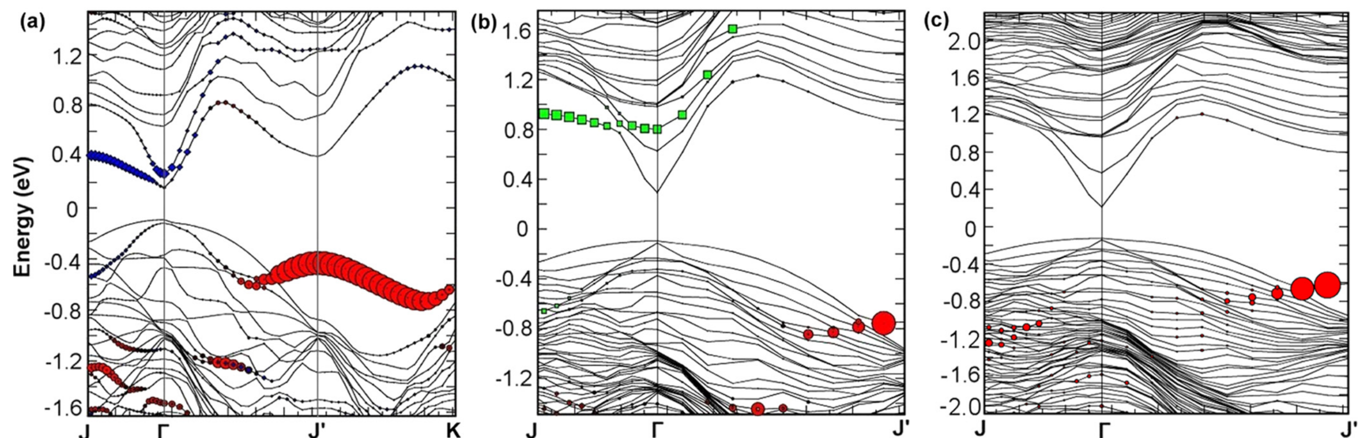


FIG. 7. (Color online) (a) Calculated band structure (LDA) along high symmetry Brillouin directions of the InSb(100)(1 × 2)-O structure with 1.0 ML of oxygen [i.e., the model in Fig. 2(b)]. The Fermi level is at 0 eV. (b) The same as (a) but calculated using HSE06 exchange-correlation functionals. (c) Hybrid exchange-correlation band structure for InSb(100)(1 × 2)-O with 2.0 ML of oxygen [i.e., the model in Fig. 2(d)].

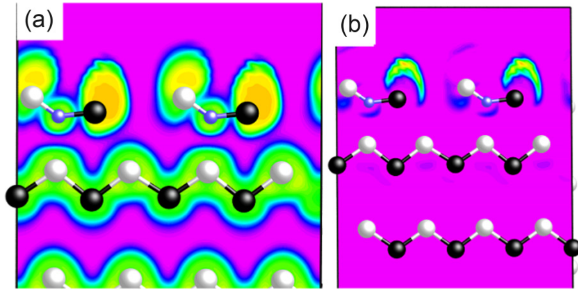


FIG. 8. (Color online) (a) Electron localization function images for the energetically favored 1.0 ML model of InSb(100)(1 × 2)-O. (b) The same as (a) but with the subtraction of the one-electron data.

by the dimer atoms for the atomic model in Fig. 1(b) with 1.0 ML of oxygen. The electron localization function generates the bonds between In and Sb at the subsurface giving some degree of localization of $sp^3$ hybridized bonding electrons. The In dangling bond also shows high ELF values. Figure 8(b) shows the relative ELF plot along the dimer plane where the one-electron ELF data is subtracted from the original ELF data. It is evident that the major changes in ELF due to removing electrons from the slab occur in the vicinity of the indium atom. The above results hold true also for the other stable models with the increased oxygen amount up to 2.0 ML.

Thus, the semiconducting band structure of the InSb(100)(1 × 2)-O surface is obtained here with the occupied indium dangling bonds. This is a striking result: As described by the electron counting model (ECM), the semiconducting nature of adsorbate-containing III-V surfaces is obtained via the structure where dangling bonds of the electropositive III atoms become empty while bonds of the electronegative V atoms become fully occupied because the former bond level locates in the conduction band and the latter in the valence band [36,37]. The top indium-related weights for the bands are illustrated by red circles in Fig. 7, and the highest weight is found at the valence band near the $J'$ point. In short, the oxidation significantly lowers the In dangling-bond energy such that the level becomes occupied, contradicting the common knowledge.

Further insight can be gained by analyzing the core-level photoemission from the InSb(100)(1 × 2)-O surface. The energy shifts, so-called core level shifts (CLS), have been extensively used for studying oxide/III-V interfaces, in particular, for determining whether III-V interfaces have been oxidized, and if so, to which extent. Simultaneously, the CLS analysis provides a stringent test for the atomic models, which should reproduce the spectra for all three elements In, Sb, and O.

Figure 9 shows the synchrotron-radiation core-level photoelectron spectra from the InSb(100)(1 × 2)-O surface. The spectra were fitted with the minimum number of the components, which was deduced with evident shoulders, asymmetries, or broadening of the pure line shapes. To obtain a justified fitting, we analyzed several spectra measured with the different photon energies: the surface sensitivity decreases in Fig. 9 from the top to bottom spectrum. It can be seen that the intensity of the bulk substrate component reasonably decreases with increasing surface sensitivity. We focus on the large (both negative and positive) shifts seen in experiments, as the smaller shifts can include errors inherent to the fitting. Table I summarizes the comparison of the measured CLS and the theoretical ones calculated with the initial-state model [38]. The agreement between the measured and theoretical CLS, calculated for the 1.0–2.0 ML models is acceptable and clearly

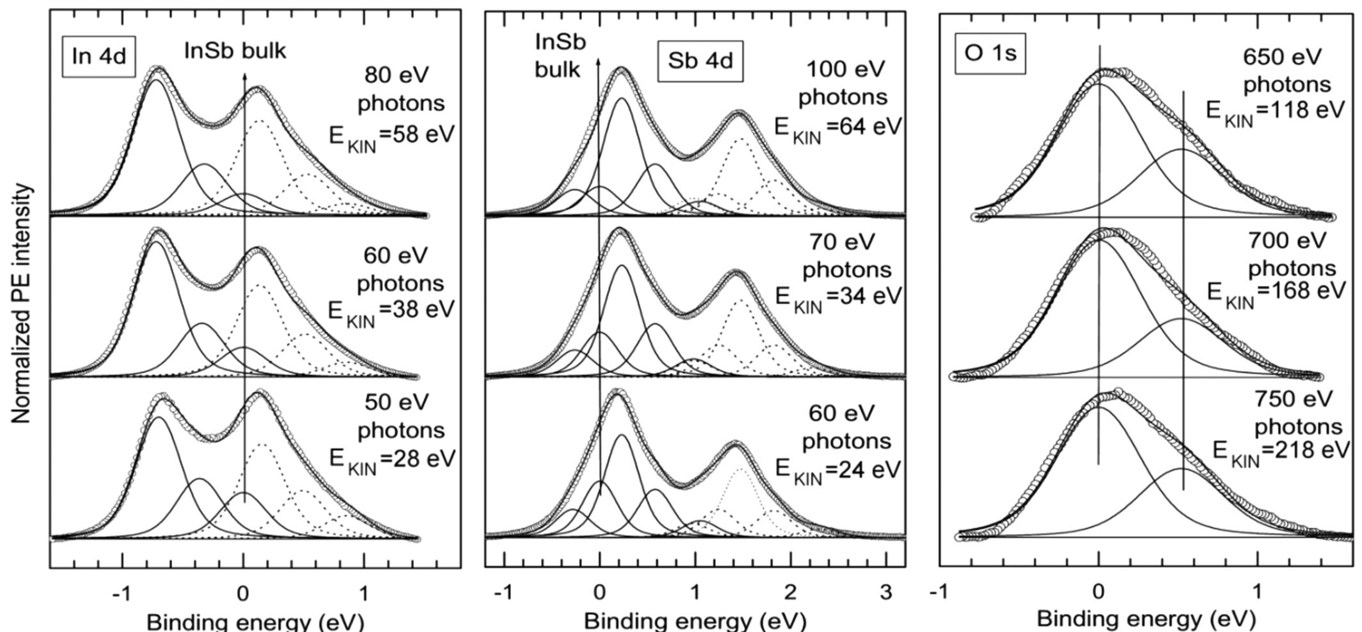


FIG. 9. (a) Measured core-level spectra from InSb(100)(1 × 2)-O and their fittings. The surface sensitivity increases toward the top spectra. For the Sb and In components, the solid lines show the $4d_{5/2}$ peaks of the doublet emission, and the dot lines mark the corresponding $4d_{3/2}$ peaks. The kinetic energies of photoelectrons ($E_{\mathrm{KIN}}$) have been estimated with the BEs of the bulk $4d_{5/2}$ peaks and lower BE component of O 1$s$.

TABLE I. Measured core-level shifts and calculated ones (in eV) for the InSb(100)($1 \times 2$)-O atomic models with the different oxygen concentrations.

| | In 4$d$ | Sb 4$d$ | O 1$s$ |
|---|---|---|---|
| Measured | −0.72, −0.36 | −0.26, +0.23, +0.58, +1.05 | −0.59, 0 |
| Model 1 [Fig. 1(a)]: 0.5 ML oxygen | −0.57, −0.06, +0.09, +0.24 | −0.13, +0.08, +0.12, +0.36, +0.92 | −0.16, 0 |
| Model 2 [Fig. 1(b)]: 1.0 ML oxygen | −0.49, +0.10, +0.25 | −0.13, +0.09, +0.13, +0.79, +1.35 | −0.58, −0.32, 0 |
| Model 3 [Fig. 1(d)]: 2.0 ML oxygen | −0.79, −0.12, +0.10 | −0.21, −0.07, +0.05, +0.97, +1.10 | −0.51, 0 |
| Model 4: 2.5 ML oxygen | −1.21, −0.24, −0.05, +0.09 | −0.07, +0.07, +0.67, +1.00 | −0.60, −0.38, −0.30, −0.23 0, |
| Model 5: 3.0 ML oxygen | −0.97, −0.17, −0.09, −0.06, +0.05, +0.11 | +0.08, +0.15, +0.37, +0.97, +1.04 | −1.09, −0.95, −0.79 |

better than for the higher and lower oxidation models, also consistent with the aforementioned results. The 0.5 ML model does not reproduce the clear O 1$s$ shifts measured, while the 2.5 and 3 ML models cause large In and O shifts, unobserved in experiments. The In 4$d$ spectra include two components shifted toward lower binding energy (BE). This is interesting because, previously, it has been commonly considered that the semiconductor oxidation causes a clear positive BE shift (+0.5 eV or higher) for the semiconductor element. The calculations reveal that the large negative shift arises from the In atoms with filled dangling bonds. Therefore, the absence of a clear positive BE shift does not guarantee the absence of oxygen and supports the benefits of using high-resolution synchrotron-radiation spectroscopy in the research of oxide/III-V interfaces.

As described above, the calculations indicate that the ordered, oxidized InSb surfaces become unstable when proceeding beyond the 2.0 ML oxidation, and the low-energy structures start to exhibit lower symmetry. Indeed, STM experiments show that a prolonged or overoxidation of InSb induces disorder and protrusion formation at the surface disturbing the symmetry, as exemplified in Figs. 10 and 11(a). The area-averaged STS spectra [Fig. 11(b)] show that the small protrusion still exhibits a band gap, yet smaller than that of the well-ordered phase [Fig. 5(a)]. The larger protrusions have, in contrast, become metallic. The calculations show that the ordered structures at 2.5–4.5 ML are metallic, but the corresponding less-ordered annealing-induced phases are semiconducting. The size of the calculated cells was $1.8 \times 0.9$ nm, i.e., ($4 \times 2$) cell. Therefore, the most likely reasons for the metallic protrusions observed in the experiments are that (i) the structure of the protrusion is metastable (not relaxed) and/or on a scale larger than the calculated cell; (ii) the stable amorphous structure of the cluster includes local point defects causing metallic states.

The results indicate the presence of a preferential oxidation window: too low but also too high oxidations can both cause the harmful gap states. To test the approach further, we synthesized InSb-based MOS capacitors (MOSCAP), including samples with various degrees of InSb preoxidations and samples without preoxidation. The *ex situ* CV experiments were performed for MOSCAP of which the schematic structure is shown in Fig. 11(c), where the "Oxidized InSb" represents different preoxidized InSb surfaces. In order to protect the oxide/InSb junctions against the air exposure during the sample transfer to a separate ALD equipment, amorphous Si cap layers were deposited on the preoxidized InSb(100) surfaces as well as on the clean InSb(100)$c(8 \times 2)$ surfaces in the same vacuum system using a homemade silicon evaporator. After the Si deposition, the samples were still heated around 400 °C in $O_2$ flow in the same chamber in order to produce a protective $SiO_x$ cap. The CV curves in Figs. 11(d) and 11(e) suggest that the interface quality of the MOSCAP containing a properly preoxidized InSb(100)($1 \times 2$)-O is better than that of an overoxidized InSb interface because the capacitance modulation is stronger (i.e., deeper C dip) for the former MOSCAP. Because the capacitance modulation is weak [as

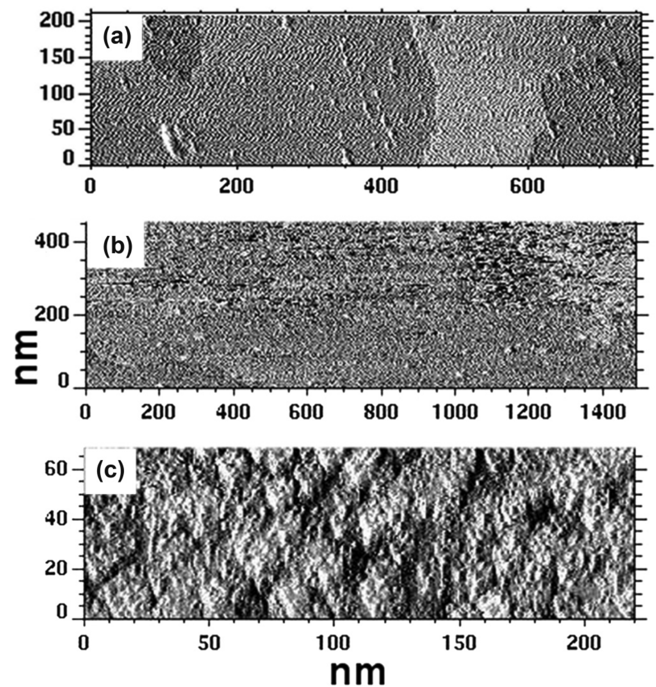


FIG. 10. (a) Large-scale STM image from a well-ordered InSb(100)($1 \times 2$)-O surface. (b) Large-scale STM image from the InSb surface after a prolonged oxidation, still showing a weak ($1 \times 2$) LEED. (c) Zoomed STM image from the same InSb surface after a prolonged oxidation showing a bumpy structure.

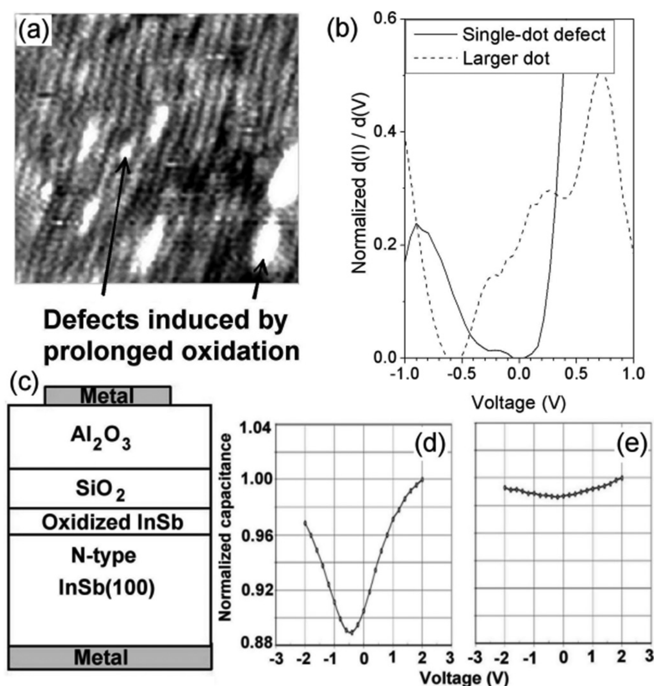


FIG. 11. STM image of the InSb(100)(1 × 2)-O surface containing defects induced by overoxidation. (b) STS curves from different defective areas. (c) Schematic MOSCAP structure. (d) 10 kHz CV curve from MOSCAP with InSb(100)(1 × 2)-O interface. (e) 10 kHz CV curve from the MOSCAP with an overoxidized InSb surface where the well-ordered (1 × 2) reconstruction has disappeared. The CV curve from the MOSCAP without the preoxidation is similar to (e).

weak as in Fig. 11(e)] also for the MOSCAP without the preoxidation, it is suggested that the postheating after the Si deposition during the Si oxidation causes the Si diffusion toward InSb, degrading the interface. This indicates further that the properly preoxidized crystalline layer can significantly decrease the harmful Si diffusion and, therefore, can be a potential buffer layer for the deposition of the Si interface passivation layer. The deposition of the Si interface passivation layer been found to be one of the most potential techniques to develop the oxide/III-V junctions for applications [7].

Concerning still the recently found benefit of the crystalline preoxidized III-V surface for the quality of the ALD-grown oxide junction [32], the common approaches to manufacture oxide/III-V junctions have been discussed. One of them includes a chemical treatment of substrates before the oxide growth with ALD. This usually involves sample transfer via air into the ALD chamber. Although the amount of substrate oxides can be decreased by this simple method, making it desirable for industry, structures of III-V interfaces are not well ordered, leading to the formation of disorder-induced defects. Therefore, the other much studied approach has been the III-V surface cleaning in vacuum using the As-decapping technique before transferring the substrate to the ALD reactor. It is still difficult to avoid the oxygen contact of III-V because the pressure is relatively high ($\sim 10^{-3}$ mbar or higher) in the standard ALD chamber and because the first metal-precursor layer hardly protects the oxygen contact of the structurally complex, reconstructed clean III-V surface. The oxygen contact leads to an uncontrolled oxidation of III-V which is very difficult or impossible to avoid in practice. The presented findings support an alternative approach: a controlled preoxidation in vacuum conditions, resulting in the 1.0–2.0 ML oxygen concentration at the crystalline III-V surface, for developing the semiconductor-based applications.

## IV. SUMMARY

In conclusion, the unveiled atomic and electronic structures of the crystalline oxidized semiconductor phases of InSb reveal a strong dependence of the electron-state formation around the semiconductor band gap on the oxygen concentration at 0.5–3.0 ML, which elucidates the previous contradictory observations about the oxidation effects. The oxide phases at 1.0–2.0 ML are clearly insulating, and their oxidation-induced electron states bands move away from the band edges. In these phases, oxidation lowers the In dangling bond level to the valence band making it occupied. Above 2.0 ML, the low-energy structures start to exhibit a disordered geometry with reduced band gaps. The findings support the presence of a preferential preoxidation window of the semiconductor surfaces concerning the development of the insulator/III-V junctions for applications.

## ACKNOWLEDGMENTS

We thank Hannu Ollila and MAX-lab staff for their assistance. This work has been supported by National Doctoral Programme in Nanoscience (M.T.), National Graduate School of Materials Physics (J.J.K.L.), Academy of Finland (Project No. 259213), and by CALIPSO (Coordinated Access to Lightsources to Promote Standards and Optimization).

[1] F. Bechstedt, *Principles of Surface Physics* (Springer, Berlin, 2003).

[2] S. Shaikhutdinov and H.-J. Freund, Adv. Mater. **25**, 49 (2013).

[3] X.-G. Wang, W. Weiss, Sh. K. Shaikhutdinov, M. Ritter, M. Petersen, F. Wagner, R. Schlögl, and M. Scheffler, Phys. Rev. Lett. **81**, 1038 (1998).

[4] H. Over, Y. D. Kim, A. P. Seitsonen, S. Wendt, E. Lundgren, M. Schmid, P. Varga, A. Morgante, and G. Ertl, Science **287**, 1474 (2000).

[5] D. Matthey, J. G. Wang, S. Wendt, J. Matthiesen, R. Schaub, E. Lægsgaard, B. Hammer, and F. Besenbacher, Science **315**, 1692 (2007).

[6] *Materials Fundamentals of Gate Dielectrics*, edited by A. A. Demkov and A. Navrotsky (Springer, Netherlands, 2005).
[7] *Fundamentals of III-V Semiconductor MOSFETs*, edited by S. Oktyabrsky and P. D. Ye (Springer, New York, 2010).
[8] A. Stierle, F. Renner, R. Streitel, H. Dosch, W. Drube, and B. C. Cowie, Science **303**, 1652 (2004).
[9] G. Kresse, M. Schmid, E. Napetschnig, M. Shishkin, and P. Varga, Science **308**, 1440 (2005).
[10] C.-L. Chang, S. K. R. S. Sankaranarayanan, D. Ruzmetov, M. H. Engelhard, E. Kaxiras, and S. Ramanathan, Phys. Rev. B **81**, 085406 (2010).
[11] *Silicon Nanocrystals: Fundamentals, Synthesis and Applications*, edited by L. Pavesi and R. Turan (Wiley-VCH, Verlag, 2010).
[12] P. Y. Delaunay, A. Hood, B. M. Nguyen, D. Hoffman, Y. Wei, and M. Razeghia, Appl. Phys. Lett. **91**, 091112 (2007).
[13] C. Y. Tseng, C. K. Lee, and C. T. Lee, Prog. Photovolt. Res. Appl. **19**, 436 (2011).
[14] V. V. Afanas'ev, A. Stesmans, and M. E. Twigg, Phys. Rev. Lett. **77**, 4206 (1996).
[15] J. H. Oh, H. W. Yeom, Y. Hagimoto, K. Ono, M. Oshima, N. Hirashita, M. Nywa, A. Toriumi, and A. Kakizaki, Phys. Rev. B **63**, 205310 (2001).
[16] Yuhai Tu and J. Tersoff, Phys. Rev. Lett. **89**, 086102 (2002).
[17] R. M. Wallace and G. D. Wilk, Crit. Rev. Solid State **28**, 231 (2003).
[18] F. Giustino, P. Umari, and A. Pasquarello, Phys. Rev. Lett. **91**, 267601 (2003).
[19] K. Sakamoto, H. M. Zhang, and R. I. G. Uhrberg, Phys. Rev. B **68**, 075302 (2003).
[20] A. Hemeryck, A. Estève, N. Richard, M. Djafari Rouhani, and Y. J. Chabal, Phys. Rev. B **79**, 035317 (2009).
[21] A. Yurtsever, M. Couillard, and D. A. Muller, Phys. Rev. Lett. **100**, 217402 (2008).
[22] T. Schmidt, A. I. Chizhik, A. M. Chizhik, K. Potrick, A. J. Meixner, and F. Huisken, Phys. Rev. B **86**, 125302 (2012).
[23] M. P. J. Punkkinen, P. Laukkanen, J. Lång, M. Kuzmin, M. Tuominen, V. Tuominen, J. Dahl, M. Pessa, M. Guina, K. Kokko, J. Sadowski, B. Johansson, I. J. Väyrynen, and L. Vitos, Phys. Rev. B **83**, 195329 (2011).
[24] M. Passlack, M. Hong, and J. P. Mannaerts, Appl. Phys. Lett. **68**, 1099 (1996).
[25] M. Hong, J. Kwo, A. R. Kortan, J. P. Mannaerts, and A. Sergent, Science **283**, 1897 (1999).
[26] T. Ashley, L. Buckle, S. Datta, M. T. Emeny, D. G. Hayes, K. P. Hilton, R. Jefferies, T. Martin, T. J. Phillips, D. J. Wallis, P. J. Wilding, and R. Chau, Electr. Lett. **43**, 777 (2007).
[27] C. L. Hinkle, M. Milojevic, B. Brennan, A. M. Sonnet, F. S. Aguirre-Tostado, G. J. Hughes, E. M. Vogel, and R. M. Wallace, Appl. Phys. Lett. **94**, 162101 (2009).
[28] H. Ko, K. Takei, R. Kapadia, S. Chuang, H. Fang, P. W. Leu, K. Ganapathi, E. Plis, H. S. Kim, S.-Y. Chen, M. Madsen, A. C. Ford, Y.-L. Chueh, S. Krishna, S. Salahuddin, and A. Javey, Nature **468**, 286 (2010).
[29] J. Wu, E. Lind, R. Timm, M. Hjort, A. Mikkelsen, and L.-E. Wernersson, Appl. Phys. Lett. **100**, 132905 (2012).
[30] L. Lin and J. Robertson, J. Vac. Sci. Technol. B **30**, 04E101 (2012).
[31] M. Scarrozza, G. Pourtois, M. Houssa, M. Heyns, and A. Stesmans, Phys. Rev. B **85**, 195307 (2012).
[32] C. H. Wang, S. W. Wang, G. Doornbos, G. Astromskas, K. Bhuwalka, R. Conteras-Guerrero, M. Edirisooriya, J. S. Rojas-Ramirez, G. Vellianitis, R. Oxland, M. C. Holland, C. H. Hsieh, P. Ramvall, E. Lind, W. C. Hsu, L.-E. Wernersson, R. Droopad, M. Passlack, and C. H. Diaz, Appl. Phys. Lett. **103**, 143510 (2013).
[33] H. Hasegawa, M. Akazawa, A. Domanowska, and B. Adamowicz, Appl. Surf. Sci. **256**, 5698 (2010).
[34] W. Wang, C. Gong, B. Shan, R. M. Wallace, and K. Cho, Appl. Phys. Lett. **98**, 232113 (2011).
[35] P. D. Ye, G. D. Wilk, B. Yang, J. Kwo, S. N. G. Chu, S. Nakahara, H.-J. L. Gossmann, J. P. Mannaerts, M. Hong, K. K. Ng, and J. Bude, Appl. Phys. Lett. **83**, 180 (2003).
[36] M. D. Pashley, Phys. Rev. B **40**, 10481 (1989).
[37] L. Zhang, E. G. Wang, Q. K. Xue, S. B. Zhang, and Z. Zhang, Phys. Rev. Lett. **97**, 126103 (2006).
[38] M. P. J. Punkkinen, P. Laukkanen, K. Kokko, M. Ropo, M. Ahola-Tuomi, I. J. Väyrynen, H. P. Komsa, T. T. Rantala, M. Pessa, M. Kuzmin, L. Vitos, J. Kollár, and B. Johansson, Phys. Rev. B **76**, 115334 (2007).